The Astrophysical Journal, 988:152 (16pp), 2025 August 1 https://doi.org/10.3847/1538-4357/ade1d7


# Connecting the Small Solar Wind Transients Observed Remotely to Their In Situ Measurement near 1 au

Shaoyu Lyu[1,2,3], Yuming Wang[1,2,4], and Christopher J. Owen[3]
[1] National Key Laboratory of Deep Space Exploration/School of Earth and Space Sciences, University of Science and Technology of China, Hefei 230026, People's Republic of China; ymwang@ustc.edu.cn
[2] CAS Center for Excellence in Comparative Planetology/CAS Key Laboratory of Geospace Environment/Mengcheng National Geophysical Observatory, University of Science and Technology of China, Hefei 230026, People's Republic of China
[3] Mullard Space Science Laboratory, University College London, Holmbury St. Mary, Dorking, Surrey, RH5 6NT, UK
[4] Collaborative Innovation Center of Astronautical Science and Technology, Hefei 230026, People's Republic of China
*Received 2025 March 15; revised 2025 May 30; accepted 2025 June 4; published 2025 July 21*

## Abstract

Based on the two-vantage observations by the COR2 coronagraphs on board the two STEREO spacecraft between 2010 January 1 and 2010 July 15, we reconstruct the three-dimensional (3D) structures of small solar wind transients in the extended corona and determine their velocities by using the CORrelation-Aided Reconstruction technique. From this data set, we select three small transient events that are predicted to arrive at the L1 point after extrapolating their 3D trajectories in the heliosphere. We find that the predicted trajectories are consistent with the heliospheric observations, and the transients are likely to have also been detected by in situ instruments at L1. The case 1 event is a streamer blob associated with high-density regions across the heliospheric current sheet detected 2 days before the occurrence of a stream interaction region (SIR). The case 2 transient is identified as the bright core of a streamer blowout coronal mass ejection entrained by an SIR, and the case 3 event is merged with the SIR-compressed outflow. The in situ properties related to these events and their ambient plasma flows are consistent with the properties of their source regions, identified after tracing their motion back to the solar surface. This work is an attempt to establish an exact connection between the coronal observations of a small solar wind transient and its in situ measurement at near 1 au and to understand the evolution of solar wind transients in the heliosphere.

*Unified Astronomy Thesaurus concepts:* Heliosphere (711); Solar corona (1483); Slow solar wind (1873)

## 1. Introduction

The solar wind has historically been divided into fast and slow solar wind (FSW and SSW), which are different in their bulk properties and composition (J. Geiss et al. 1995; R. Schwenn 2006; L. Abbo et al. 2016). Compared to the FSW, the SSW generally has larger spatial and temporal variability, containing many transient structures that originate from the Sun or form during the propagation of solar wind (N. M. Viall et al. 2021). From the white-light coronagraph images taken by the Solar and Heliospheric Observatory (SOHO) Large Angle and Spectrometric Coronagraph (G. E. Brueckner et al. 1995), J. N. R. Sheeley et al. (1997) detected a class of small solar wind transients, called "blobs," released from the cusp of coronal helmet streamers. These structures have smaller scales (about 1 $R_\odot$ in length and 0.1 $R_\odot$ in width at the distance of 3–4 $R_\odot$) than general coronal mass ejections (CMEs) and can be classified as "mesoscale" transients (G. D. Dorrian et al. 2010; N. M. Viall et al. 2021). The mesoscale structures at 1 au are defined to have spatial scales of roughly 5–10,000 Mm and temporal scales from seconds to several hours, larger than the dissipation scale at 1 au (R. J. Leamon et al. 1998) and smaller than the largest structures in the heliosphere. According to their propagation traces from the extended corona to the heliosphere, they are accelerated to the characteristic SSW velocity, which suggests that they are possibly one of the sources of the transient SSW in the heliosphere (J. N. R. Sheeley et al. 1997; Y. M. Y. M. Wang et al. 1998; N. R. Sheeley et al. 1999). Simultaneous observations from the twin Solar Terrestrial Relations Observatory (STEREO; M. L. Kaiser et al. 2008) spacecraft show that the streamer blobs may have the configuration of magnetic flux ropes (N. R. Sheeley et al. 2009). Some observations and magnetohydrodynamic (MHD) simulations suggest that blobs can be released by the pinch-off magnetic reconnection at the cusp of streamer loops (E. Endeve et al. 2003, 2004; J. N. R. Sheeley & Y. M. Wang 2007; Y. Chen et al. 2009; N. R. Sheeley et al. 2009; E. Sanchez-Diaz et al. 2017b; A. K. Higginson & B. J. Lynch 2018; V. Reville et al. 2020, 2022). E. Sanchez-Diaz et al. (2017b) associated the release of blobs with the inflows of plasma observed by coronagraphs, suggesting that they are released by intermittent magnetic reconnection triggered by the tearing instability (G. Einaudi et al. 1999) in the solar corona. H. Li et al. (2024) investigated the formation and acceleration process of a streamer blob below 2 $R_\odot$, suggesting that it is formed by interchange reconnection in the flanks of the streamer. Another kind of mesoscale transient, with smaller scales, is the periodic density structure, which has been observed through in situ measurements at 1 au and in remote observations from the corona to the heliosphere (L. Kepko et al. 2002, 2016, 2020; L. Kepko & H. E. Spence 2003; N. M. Viall et al. 2008, 2009a, 2009b, 2010, 2015; S. Di Matteo et al. 2019; I. Gershkovich et al. 2023; R. Ventura et al. 2023). These are pressure balance structures with density fluctuations anticorrelated with magnetic field fluctuations and detected with a periodicity of $<100$ minutes in the in situ measurements of the

solar wind. This is much lower than the average period of 19.5 hr for blobs (E. Sanchez-Diaz et al. 2017a). Some studies (Y. M. Wang et al. 1998; J. K. Edmondson 2012; D. Baker et al. 2023; L. P. Chitta et al. 2023; N. E. Raouafi et al. 2023) suggest that many small transients widely distributed in the SSW are released by interchange reconnection between the open field and closed loops.

The release and formation of these small transients is an important cause of the highly variable outflows in the SSW. E. Sanchez-Diaz et al. (2017a, 2019) divided the in situ features of blobs into five scenarios associated with different trajectories of a spacecraft crossing the heliospheric plasma sheet (HPS) in the SSW, which matches their hypothesis that the HPS is formed of continuous dense blobs separated by magnetic flux ropes. P. C. Liewer et al. (2024) also detected the occurrence of continual flux ropes near the heliospheric current sheet (HCS), which is observed by the WISPR imagers on board the Parker Solar Probe (PSP; N. J. Fox et al. 2016). N. Alzate et al. (2024) tracked propagating disturbances detected in the low corona (N. Alzate et al. 2021) along different nonradial paths of streamers (N. Alzate et al. 2023) to the extended corona and revealed that they can be classified into fast and slow transients formed at different locations and released as part of the solar wind streams. These transient structures may contain the imprints of the physical processes related to coronal heating and release and acceleration of the solar wind (N. M. Viall & J. E. Borovsky 2020), so further investigating the origin and evolution of the transients is necessary.

To study the overall propagation of transients from the Sun into interplanetary space, the combination of in situ and remote observations is necessary. Streamer blobs containing plasma with high $\beta$ values have previously been detected by in situ instrumentation (N. U. Crooker et al. 1996, 2004; E. K. J. Kilpua et al. 2009), and their propagation through the heliosphere can be observed directly in heliospheric images, particularly from the Heliospheric Imager (HI; C. J. Eyles et al. 2009) on board STEREO (A. P. Rouillard et al. 2009, 2010; N. R. Sheeley & A. P. Rouillard 2010). The remote observation of small transients by HI is limited as the density of structures decreases with radial distance, and it is also limited by other constraints imposed by Thomson scattering (E. E. Sanchez-Diaz et al. 2019). However, some blobs propagating into interplanetary space can be observed by remote observations, especially when they are compressed by FSW and entrained by stream interaction regions (SIRs) during their propagation (A. P. Rouillard et al. 2008, 2010). Meanwhile, the outflows containing the small transients observed in situ may be traced from the spacecraft back to the corona and the Sun by the ballistic back-mapping technique (M. Neugebauer et al. 1998, 2002; Y. M. Wang et al. 1998; A. R. Macneil et al. 2019, 2022; Y. C. M. Liu et al. 2020; B. J. Lynch et al. 2023; C. Hou et al. 2024a, 2024b). However, the ballistic method may introduce an uncertainty of about 10° in longitude (J. T. Nolte & E. C. Roelof 1973), and the inward MHD mapping toward the Sun (V. J. Pizzo 1981; P. Riley et al. 1999) suggests that the ballistic-mapping result is inadequate when tracing the leading edge of FSW streams. It is difficult to directly link a small transient observed remotely to its in situ features if its overall trajectory to the spacecraft is not observed, unless we can successfully extrapolate its trajectory in three-dimensional (3D) space to the position of a spacecraft.

In previous studies (X. L. Li et al. 2018; X. Li et al. 2020, 2021, 2023; S. Lyu et al. 2020, 2021), we studied the 3D positions, velocities, and structures of solar wind transients during their propagation in the heliosphere using the CORrelation-Aided Reconstruction (CORAR) technique, which is based on the simultaneous observations from two vantages. This technique had been further developed for the application of coronagraph images (S. Lyu et al. 2023) and used to study the evolution and origins of small transients in the extended corona (S. Lyu et al. 2024). Here, we use the extrapolated trajectories of small transients detected by the CORAR technique to make a connection with the in situ measurements by the 1 au spacecraft and to study their propagation and properties in interplanetary space. We introduce the data and methodology in Section 2, present examples of the transients that can be traced to 1 au with their related in situ features in Section 3, and discuss their properties and origins in Section 4. Our conclusions are summarized in Section 5.

## 2. Data and Method

### 2.1. Data from Remote Observation and In Situ Measurement

The remote observation data used for our study come from the Sun Earth Connection Coronal and Heliospheric Investigation (SECCHI; R. A. Howard et al. 2008) suite on board STEREO. The two STEREO observatories provide stereoscopic measurements to study the Sun and solar wind. The SECCHI suite contains an extreme-ultraviolet imager, two visible-light coronagraphs (COR1 and COR2), and two heliospheric telescopes (HI-1 and HI-2) to study the propagation of solar wind from the Sun through the corona and interplanetary space to the Earth. COR2 observes the outer corona at 2.5–15 $R_\odot$ from the Sun, and HI-1 traces transient outflows up to 60 $R_\odot$ in the solar system. The COR2 images are applied to derive the 3D position and velocity of transient events detected in the corona. We use the heliospheric images from the HI-1 instrument to follow the trajectories of the transients into the heliosphere, and we use the HI-2 images to evaluate the tracking results from 60 $R_\odot$ to 1 au. The images are processed by subtracting the background images downloaded from the SolarSoft database to restrain the F corona and performing median filtering to restrain the star field and stray light (C. E. DeForest et al. 2011, 2018; T. A. Howard & C. E. DeForest 2012; C. E. DeForest & T. A. Howard 2015). In particular, the persistent coronal streamers are removed from the COR2 images to highlight the transients.

The in situ measurements used for our study come from data recorded by the Advanced Composition Explorer (ACE) and WIND, which are located near the L1 Lagrange point on the Sun–Earth line. The ACE mission has been operating continuously since 1998 to return information on the particles in the solar wind. Here we investigate the 1 minute averaged bulk properties of the solar wind outflow and the 1 minute pitch-angle (PA) distributions of suprathermal electrons using data from the Solar Wind Electron Proton Alpha Monitor (D. J. McComas et al. 1998) on board ACE. Meanwhile, we study the 16 s magnetic field recorded by the Magnetic Field Experiment (C. W. Smith et al. 1998) and the 1 hr ion parameters of charge states ($O^{7+}/O^{6+}$) and first ionization potential (FIP) bias (Fe/O) measured by the Solar Wind Ion Composition Spectrometer (G. Gloeckler et al. 1998) on board ACE. To mitigate for data gaps in the ACE measurement, we also make use of the magnetic field measured by the WIND

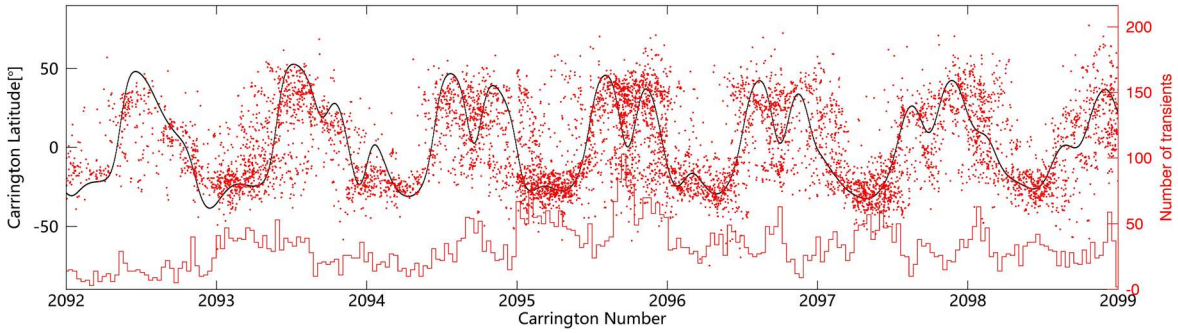


**Figure 1.** The Carrington latitude (red points) and frequency histogram (red lines) of CORAR-detected transients over different Carrington periods. The black line represents the PIL provided by the National Solar Observatory Integrated Synoptic Program. We exclude the transients belonging to the CME lists generated by CACTus (E. Robbrecht et al. 2009).

Magnetic Field Investigation (R. P. Lepping et al. 1995) and the solar wind properties measured by the WIND Solar Wind Experiment (K. W. Ogilvie et al. 1995) instruments. The time resolution of these parameters is about 1.5 minutes.

### 2.2. The Transients Detected by the CORAR Technique

The purpose of the CORAR method is to identify and reconstruct the 3D structures of transients through triangulation, based on simultaneous observations from two distinct points. It recognizes the 3D position and shape of transients by calculating the correlation coefficients of different partial regions on the images from two spacecraft. Further details of the method are described in our previous studies (X. L. Li et al. 2018; X. Li et al. 2020, 2021, 2023; S. Lyu et al. 2020, 2021, 2023). We also calculate the velocity of transients by their positions in consecutive images and generate a list of reconstructed transient events. In the final data set, we remove any large-scale, unreal, or incomplete structures reconstructed by CORAR, according to the morphology and continuity of reconstructed transients (S. Lyu et al. 2024).

A list of 14,194 transient events at small scales is generated from the COR2 observations between 2010 January 1 and 2010 July 15. Of these, 8131 are not associated with large CME events, as indicated by the CME lists generated by CACTus (E. Robbrecht et al. 2009). During this interval, the separation angle between the two STEREO spacecraft is between 130° and 150°, which is conducive to the application of CORAR on the coronagraph images (S. Lyu et al. 2023). Compared with the data set in S. Lyu et al. (2024), there are more events in the current list because it also contains transients moving away from the Earth or toward high-latitude interplanetary space, up to 80° from the ecliptic plane. In addition, we retain the events that are detected by CORAR but not obvious in the images, which were discarded in S. Lyu et al. (2024). Figure 1 presents the Carrington latitude and frequency histogram of transient events recognized by the CORAR technique over different Carrington periods. Most events are located near the HCS, which is indicated by the black polarity inversion line (PIL) derived from the Potential Field Source Surface (PFSS) extrapolation of photospheric magnetic fields (C. J. Schrijver & M. L. DeRosa 2003). During several Carrington periods, the number of detected events is relatively lower when the current sheet is oblique from the equator. This suggests that it is more probable to observe small transient events near the HCS from two points of view simultaneously when the HCS is approximately parallel to the equatorial plane.

### 2.3. Connecting Transients to the In Situ Observatory

To extrapolate the 3D trajectory of a transient from the corona into the heliosphere, we assume that the direction of motion of the transient remains constant, and reproject its position in heliospheric images into 3D space. Here we generate time-elongation maps (J maps) from the STEREO-A COR2 (COR2-A) and HI-1 images to manually locate the position of the core and edges of a transient observed on 2010 January 13, as illustrated in Figure 2(a). The J map is derived by summing the pixels at the same height within the azimuthal width of the transient. To estimate the velocity profile of the transient in the heliosphere, we fit the velocity of its core calculated by its 3D location with the equation

$$V = V_0 + V_1\left(1 - e^{-\frac{r-r_1}{r_a}}\right)^n, \quad r < 30\,R_\odot. \tag{1}$$

The equation is applied in reference to the acceleration profile of the transient structures described in J. N. R. Sheeley et al. (1997). Figure 2(b) displays the fitted profile, accompanied by a 90% prediction band for this transient. The velocity profiles for the leading and trailing edges are derived from the fitted profile by the ratio between the measured velocities of the core and the edges. The measured velocity at 15–17 $R_\odot$ exceeds the prediction band, which is due to the uncertainty of the position measurement near the boundary between the COR2 and HI-1 images.

In light of the residual acceleration of the interplanetary solar wind (P. Riley & R. Lionello 2011; M. J. Owens & P. Riley 2017; L. Barnard & M. Owens 2022; K. A. Bunting & H. Morgan 2023; K. A. Bunting et al. 2024), we employ the following equation to extrapolate the radial propagation of the transient to 1 au:

$$V = V_{30\,R_\odot} + \alpha V_{30\,R_\odot}\left(1 - e^{-\frac{r-30\,R_\odot}{50\,R_\odot}}\right), \quad r > 30\,R_\odot. \tag{2}$$

The parameter $\alpha$ can be derived from the continuity of the boundary condition. Based on this method, we trace transients to the location of a spacecraft as presented in the next section and examine if associated features can be identified in in situ data.

## 3. Results

### 3.1. Selection of Transient Events from the Reconstruction Data Set

In order to find potential transients detected by the spacecraft in the vicinity of 1 au, we select events satisfying

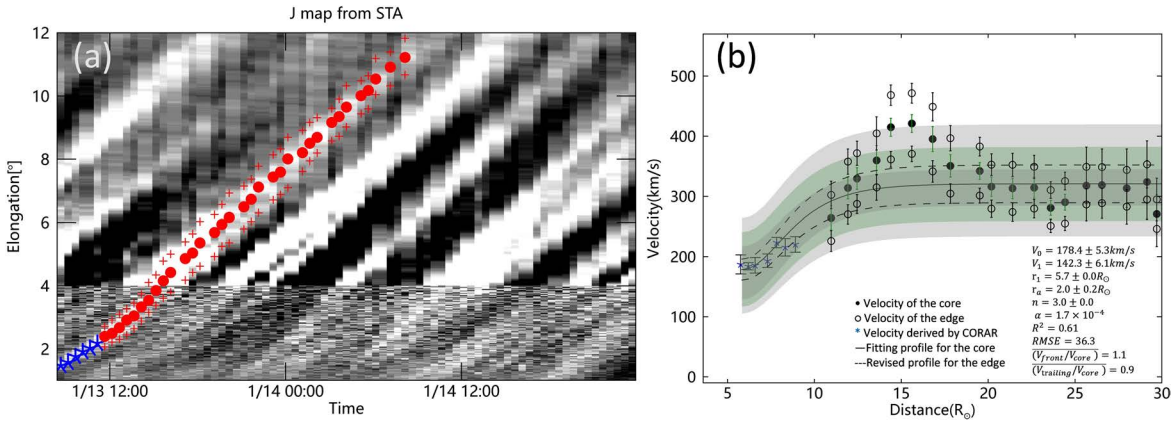


**Figure 2.** Panel (a): the J map applied for calculating the position and velocity of the core and edges of the transient event observed on 2010 January 13. The blue asterisks represent the position derived from the CORAR technique. The red points and plus signs represent the location of the center and edges of the transient, respectively. Panel (b): the fitted profile (black solid line) of the measured velocity of the transient center, marked by the black solid points and blue asterisks, with the 90% prediction band (green region). The fitted parameters are shown in the lower part of this panel. The black dashed lines with gray bands represent the estimated velocity profiles and uncertainty boundaries of the leading and trailing edges of the transient.

the following criteria: (1) the reconstructed structure of a transient should be possible for >2 hr, (2) the propagating direction is determined to be between −5° and 5° in latitude and between 0° and 10° in longitude in heliocentric ecliptic Earth (HEE) coordinates, and (3) no large-scale CME appears within 12 hr, and the transient is not overtaken by a large CME. The longitudinal range in the criteria is >0° in consideration of the orbital motion of the Earth as the transients propagate. From the overall data set, three events are selected for further investigation (Table 1). The COR2 images depicting the three cases are presented in Figure 3. The case 1 event is a small transient released from the northern part of the southern streamer region on 2010 January 13, according to the original coronagraph observations (panels (a1)−(a4) in Figure 3). The reconstructed structure in 3D space has an average width of 7.8° in latitude and 16.8° in longitude and an aspect ratio of 1.9 between radial length and latitudinal width, and it propagates toward the direction of -1.8° in latitude and 5.0° in longitude. In comparison to case 1, the transient event in case 2 is more discernible within the COR2 field of view (FOV) and appears to be a bright part of the loop-like structure ejected from the southern streamer boundary on 2010 May 14 (panels (b1)–(b4) in Figure 3). Its reconstructed structure has an average width of 16.0° in latitude, larger than the latitudinal width of the reconstructed transient in case 1, and 17.6° in longitude. The radial size is approximately equivalent to the latitudinal width, and it propagates in a direction of approximately -4.3° in latitude and 0.8° in longitude. From panels (c1)–(c4) in Figure 3, the case 3 event forms part of a larger-scale outflow with enhanced density, propagating along the northern boundary of the southern streamer on 2010 July 9. The mean width of the reconstructed transient is about 7.2° in latitude and 22.2° in longitude, and its aspect ratio is approximately 1.7. Its propagating direction is about −1.2° in latitude and 4.3° in longitude, while the 1$\sigma$ uncertainty in longitude is larger than 3° because of its longitudinal shift during propagation.

To test the accuracy of the reconstruction by the CORAR method, a comparison was undertaken between the reconstructed structure in case 1 and the forward-modeling result derived from the elliptical model provided in the SolarSoftWare system. Figures 4(b) and (c) illustrate that the size of the structure reconstructed by our CORAR technique is larger than the structure estimated by the model in latitude and longitude, while the position and radial size of the transient derived by our method are consistent with the forward-modeling result in Figure 4(a). This validates the assumption of the radial propagation for tracing small transients into the heliosphere from the single-vantage observation.

### 3.2. Comparison of Predicted Trajectories with HI-2 Observations

Based on the tracing method outlined in Section 2.3, the trajectory of transients in 3D space can be estimated. Figure 5(a) illustrates the predicted trajectory of the event in case 1 in the coordinate system rotating with the Sun. The origin of this coordinate system is the center of the Sun. Its *Z*-axis points to the north pole, and its *X*-axis points to 0° in Carrington longitude. The shaded region indicates the width of the structure of this event, estimated by the CORAR technique, in longitude of this rotating coordinate system. The trajectory exhibits a slight angular deviation of approximately 1.7° from the direction toward the Earth. Figures 5(b) and (c) display the J maps along the Sun–Earth connection line extending to 1 au, as extracted from STEREO images. These J maps are different from the map mentioned in Section 2.2, which is derived along the line connecting the transient and the Sun. The predicted trajectory of the center of the event, along with the uncertainty in estimating the traces of its core and edges, is also projected onto these J maps. In the STEREO-A FOV, the estimated trace of the core of the transient is consistent with the observation, arriving at L1 on 2010 January 18 11:52 UTC, while the features of the transient observed by HI are not apparent above 120 $R_\odot$ from the Sun. The uncertainty in the predicted arrival time may exceed 1 day. This is calculated from the 90% prediction band of the measured velocity profile. From the remote observations taken by STEREO-A (panels (d1)–(d6) in Figure 5), it can be seen that a small structure is located near the predicted position and propagates ahead of an outflow with enhanced brightness from 2010 January 16. This density-enhanced outflow is evident in the J map and is expected to reach L1 on January 20. It appears to be the emergence of successive blobs entrained by the same SIR (N. R. Sheeley & A. P. Rouillard 2010). The trajectory observed by STEREO-B

**Table 1**
The List of the Transient Events Selected for This Study

| Event No. | Time of Reconstruction | HEE Longitude with $\pm\sigma$ (deg) | HEE Latitude with $\pm\sigma$ (deg) | 3D Size | | |
|---|---|---|---|---|---|---|
| | | | | Latitude (deg) | Longitude (deg) | Aspect Ratio between Radial and Latitudinal Size |
| 1 | 2010/01/13 07:54–10:54 | $5.0 \pm 0.9$ | $-1.8 \pm 0.3$ | $7.8 \pm 0.8$ | $16.8 \pm 4.0$ | $1.9 \pm 0.3$ |
| 2 | 2010/05/14 01:24–03:54 | $0.8 \pm 0.3$ | $-4.3 \pm 0.3$ | $16.0 \pm 2.0$ | $17.6 \pm 5.8$ | $1.1 \pm 0.1$ |
| 3 | 2010/06/09 12:54–17:54 | $4.3 \pm 3.5$ | $-1.2 \pm 0.2$ | $7.2 \pm 1.6$ | $22.2 \pm 8.8$ | $1.7 \pm 0.5$ |

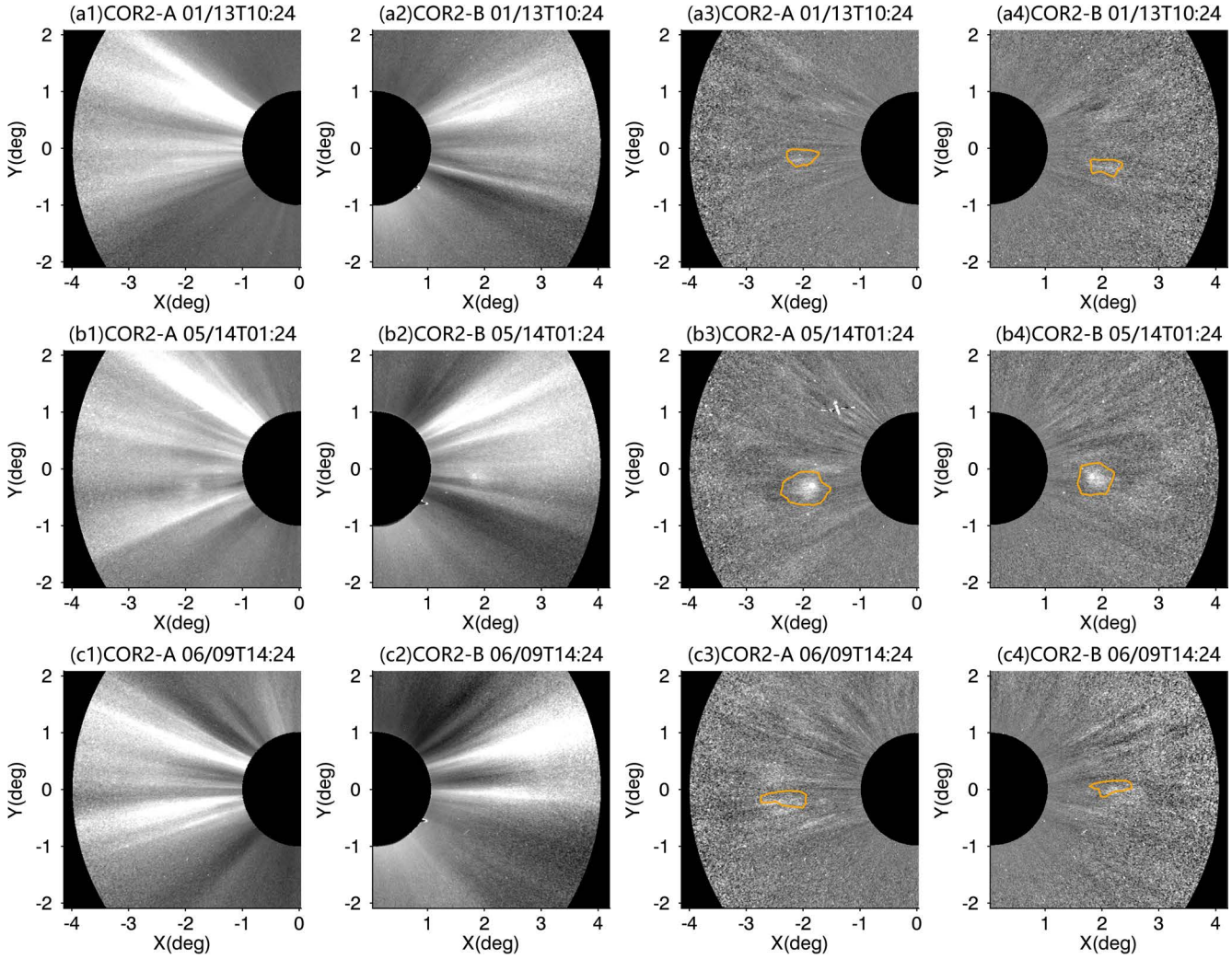


**Figure 3.** The observations of the three selected transient events by COR2-A and COR2-B. The images in the first two columns contain the quiescent streamer structures, which are removed in the images in the last two columns. The reconstructed structures of three events are projected on the images in the last two columns, as shown by the regions outlined in yellow.

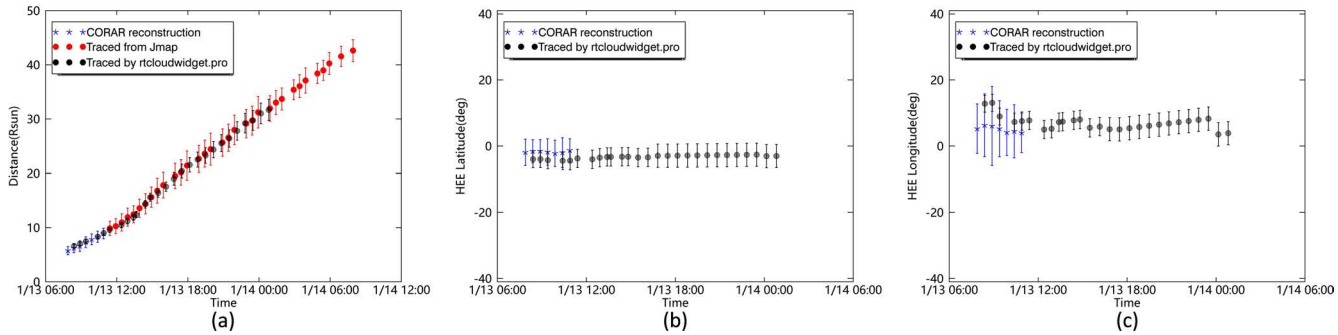


**Figure 4.** The position and size of the CORAR-reconstructed structure (blue points with error bars) and the forward-modeling structure (black points with error bars). Panel (a) illustrates the comparison in radial distance, panel (b) is latitude, and panel (c) is longitude in our case 1. The red points in panel (a) represent the trajectory of the transient extrapolated by the tracing method in Section 2.3.

shown in Figure 5(c) does not correspond precisely to the predicted path, but it is situated within the uncertainty range.

Figure 6(a) illustrates the predicted trajectory of the event in case 2. Its direction has undergone a shift of approximately 4.8° in longitude and 3.7° in latitude from the Sun–Earth line, while the reconstructed transient is likely to be detected at L1 given its angular scale. As illustrated in Figure 6(b), the STEREO-A J map reveals an apparent trajectory reaching the L1 point on May 19, which is consistent with the predicted trajectory of the center of this event. The estimated time of its arrival at L1 is 2010 May 19 09:43 UTC. The latitudinal width of the transient observed by HI is larger than that observed by COR2 and expands into a large loop-like structure as it progresses further into the heliosphere (see panels (c) and (d) in Figure 6). This event is not discernible in the STEREO-B J map, which is not included in Figure 6.

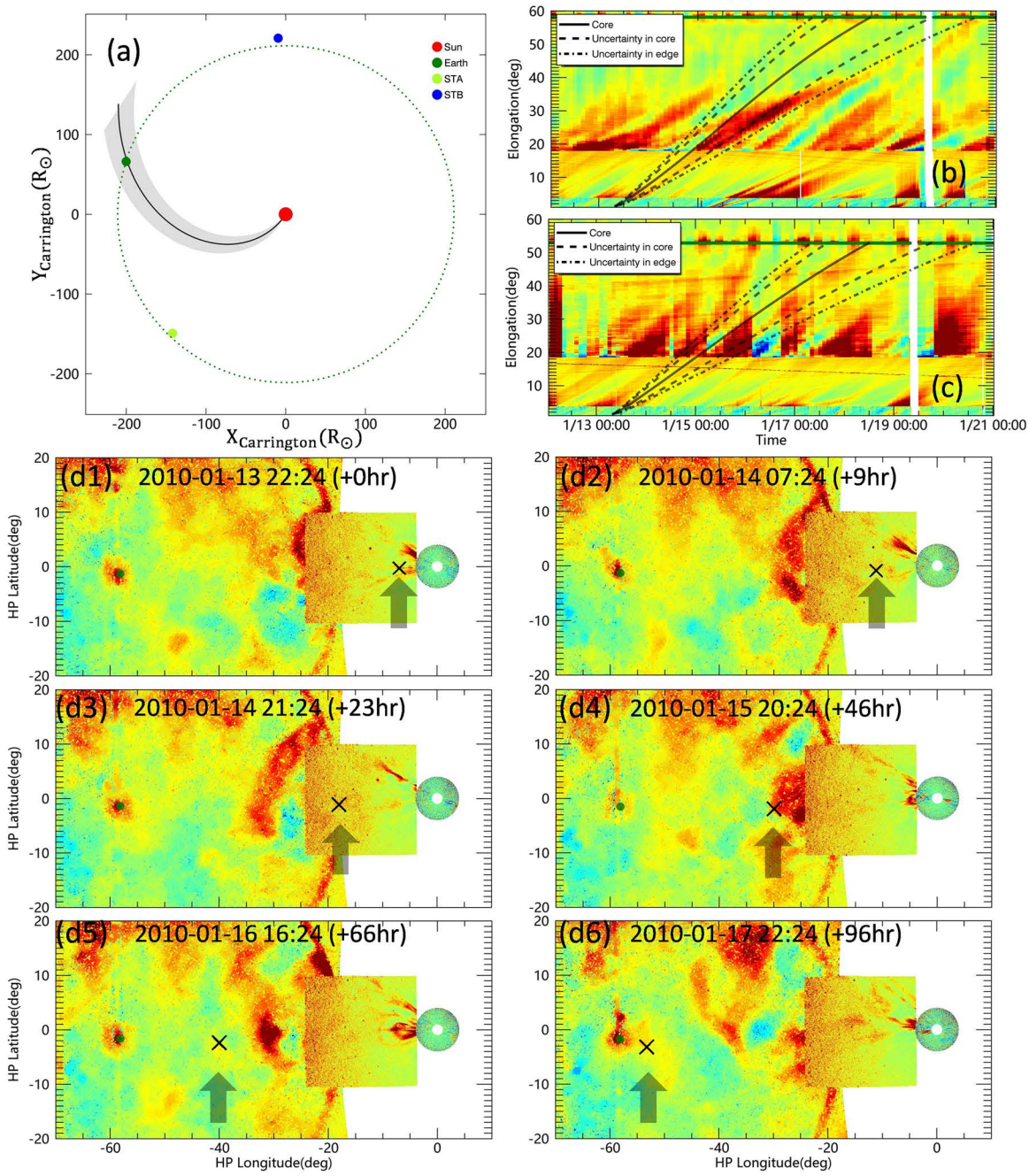


**Figure 5.** Panel (a): the predicted trace of the case 1 event in the *X*–*Y* plane of the frame rotating with Sun. The *Z*-axis of the coordinate system points to the north pole of the Sun, and the *X*-axis ($X_{\rm Carrington}$) points to 0° in Carrington longitude. The shaded region marks the longitudinal width of the reconstructed transient. Panel (b): the J map along the Sun–Earth line generated from STEREO-A images. The predicted trajectory of the center of the transient, along with its uncertainty boundaries calculated from the 90% prediction band of the velocity profile, is projected on the map, and the uncertainty boundaries for the edges of the transient are also displayed. The horizontal green line at the top of the figure represents the position of the L1 point. Panel (c): the J map along the Sun–Earth line generated from STEREO-B images. Panels (d1)–(d6): the white-light observation of the case 1 event in the corona and heliosphere by COR2, HI-1, and HI-2 on board STEREO-A. The time of observation is displayed, and the black cross pointed to by the arrow marks the predicted position of the event. The position of L1 is indicated by a green point.

Figure 7 illustrates the forecast trajectory of the case 3 event in comparison with the HI observation by STEREO-A. The STEREO-B J map is not shown since the trajectory of the event is not discernible. The propagating direction is $<1.3°$ relative to the Sun–Earth line. The predicted arrival at L1 is 2010 June 14 18:48 UTC. This is ∼16 hr earlier than the trace of the event suggested by the J map, although the arrival time of the observed trace remains within the range of uncertainty. Additionally, the J map illustrates other transients occurring between June 10 and 15, with their paths appearing to converge with that of the case 3 event at a greater distance from the Sun. As illustrated in Figures 7(c)−(e), the HI observations reveal the presence of two large structures with enhanced brightness, discernible in the HI-2 FOV and not in that of HI-1. The first large structure appears to be caught up with a fast CME upon its arrival at the Earth on June 12 21:00 UTC, while the CME is not observed in the HI-1 and COR2 FOV. It suggests that the direction of the fast CME is different from the case 3 event, so the propagation of the CME

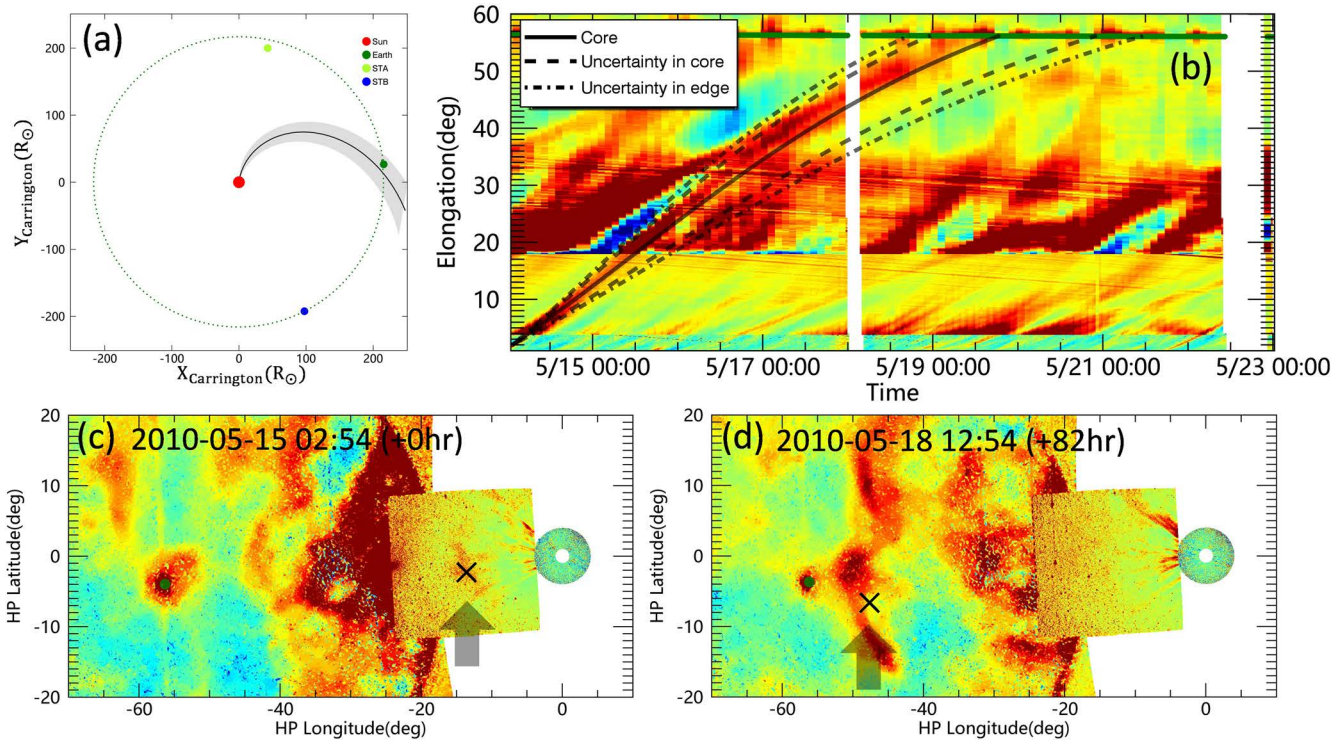


**Figure 6.** Panel (a): the predicted trajectory of the case 2 event. Panel (b): the J map along the Sun–Earth line generated from STEREO-A images, along with the predicted trajectory projected on the map. Panels (c) and (d): the remote observation of the propagation of the case 2 event by STEREO-A.

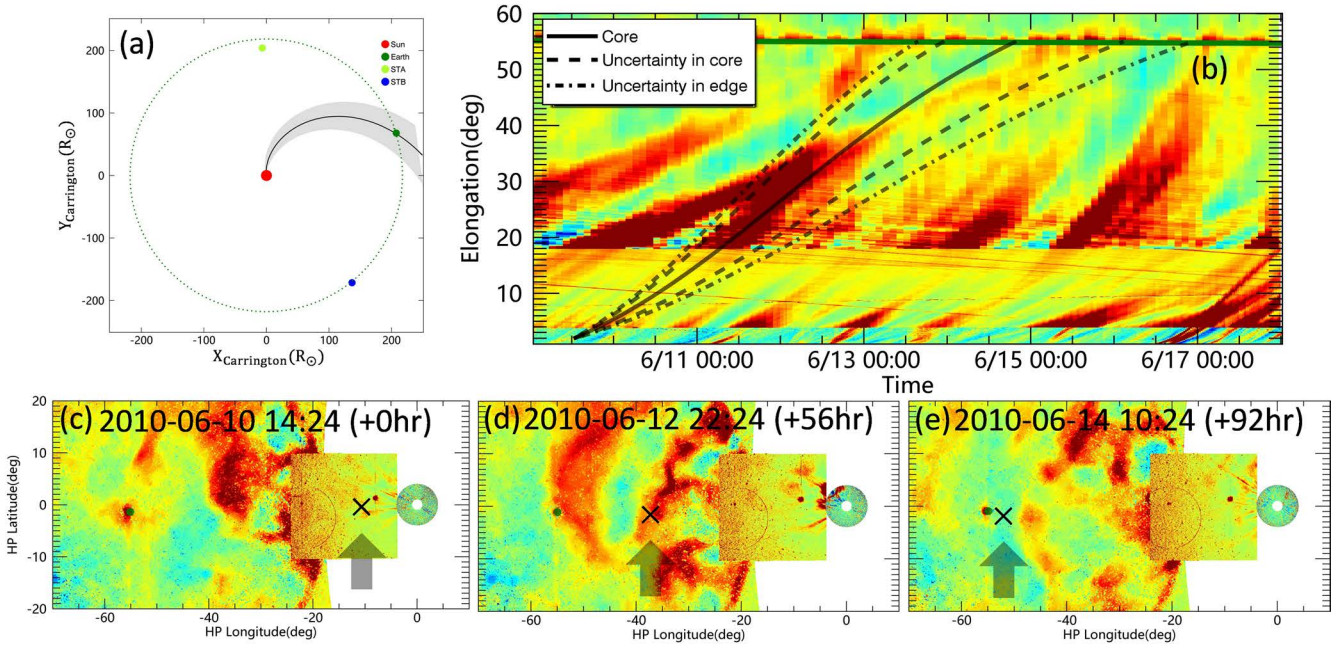


**Figure 7.** Panel (a): the predicted trajectory of the case 3 event. Panel (b): the J map along the Sun–Earth line generated from STEREO-A images, along with the predicted trajectory projected on the map. Panels (c)–(e): the remote observation of the propagation of the event by STEREO-A.

has no impact on the event we study. The predicted position of the case 3 event is situated near the second prominent structure, which faded and decelerated in the J map, and then it is anticipated to surpass this large structure after 12:00 on June 13.

### *3.3. Tracing Transients to L1*

In this section, we present the properties likely associated with these transients, as observed in situ around the predicted time of their arrival at L1. This is a crucial aspect for investigating their connection to the remote observations and the subsequent evolution of transients following propagation.

Figure 8 presents the in situ observation of the solar wind recorded at ACE and WIND during the possible passage of the event in case 1. The three points in Figure 8(a) label the predicted velocity and arrival time of the leading edge (blue point P1: 2010 January 18 00:49 UTC), center (orange point

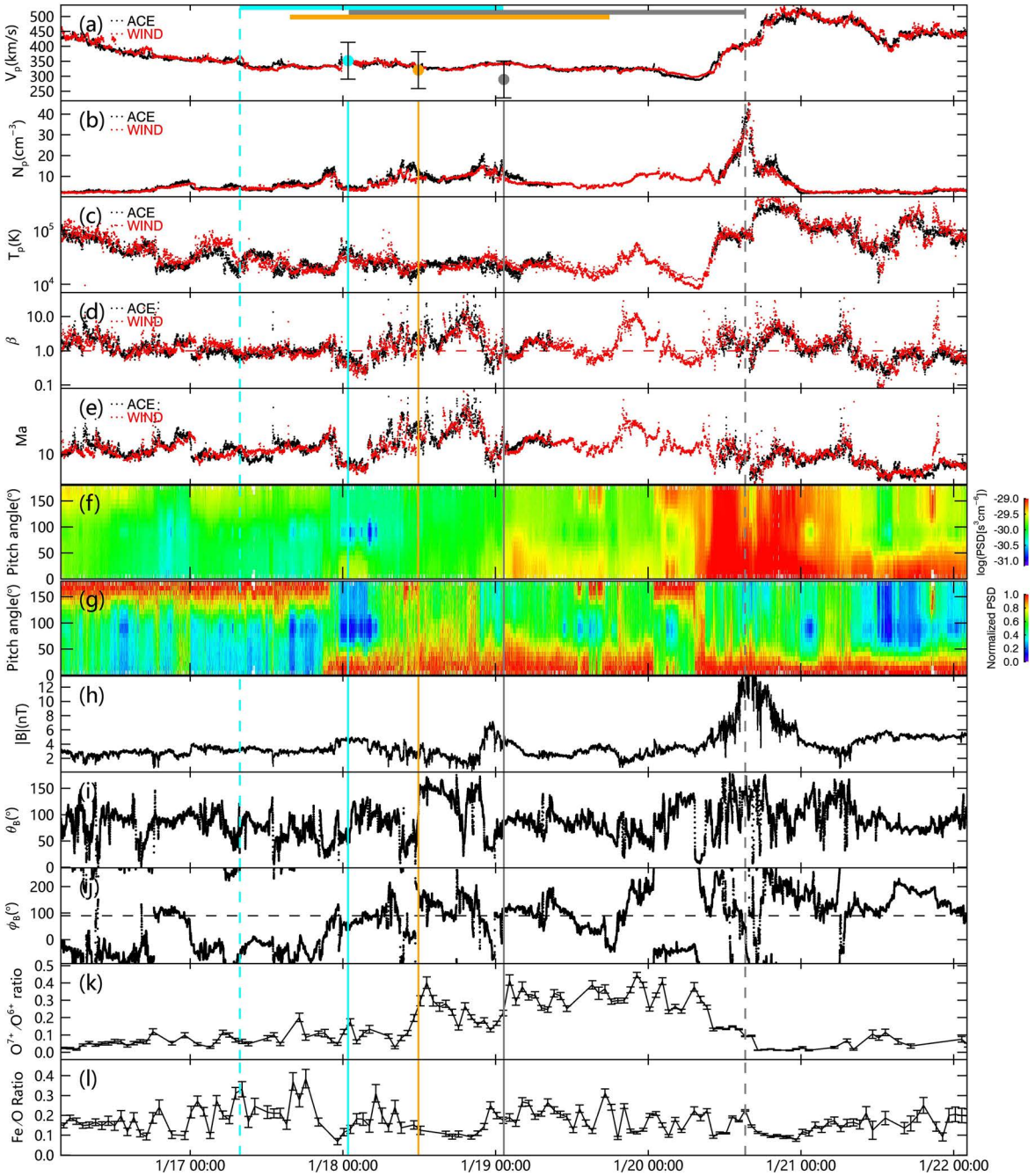


**Figure 8.** The solar wind properties measured by ACE and WIND around the predicted arrival time of the case 1 transient. From top to bottom, the following quantities are plotted as a function of time: (a) velocity, (b) proton density, (c) proton temperature, (d) plasma $\beta$, (e) Alfvénic Mach number, (f) PA distribution of the PSD of suprathermal electrons at around 272 eV, (g) PA distribution of suprathermal electrons normalized by the maximum PSD during the same time period, (h) magnetic field magnitude, (i) elevation angle of the magnetic field, (j) azimuth angle of the magnetic field, (k) $O^{7+}/O^{6+}$ ratio, and (l) Fe/O ratio. Panels (f)–(l) utilize the data from ACE only. The three points in panel (a), named P1, P2, and P3, respectively, label the predicted velocity and arrival time of the leading edge, center, and trailing edge of the transient, and their uncertainty ranges are marked by the bars with the same colors at the top of the figure. The magnetic field directions shown in panels (i) and (j) are calculated in GSE coordinates, and the area below (above) the dashed line in panel (j) represents that the direction of the magnetic field points sunward (antisunward), defined as negative (positive) polarity of the magnetic field.

P2: 2010 January 18 11:52 UTC), and trailing edge (gray point P3: 2010 January 19 01:18 UTC) of this transient, and their uncertainty ranges are marked by the bars with the same colors at the top of the figure. The direction of the magnetic field is presented in geocentric solar ecliptic (GSE) coordinates. We define that the magnetic field has a negative/positive polarity if the radial direction of the magnetic field is oriented sunward/antisunward. The velocity measured in situ near the predicted arrival time is between 310 and 350 km s$^{-1}$, which is consistent with the predicted velocities. We find three peaks in density, each lasting several hours and occurring in proximity to the predicted P1, P2, and P3, respectively, indicating their possible relationship with the case 1 event and its surrounding transient flow. The first peak near P1 is accompanied by an increase in proton temperature ($T_p$), a brief peak in plasma $\beta$ and Alfvénic Mach number ($M_a$), a reversal of the PA distribution of suprathermal electrons, a shift in magnetic field direction from negative to positive polarity, and a decrease in

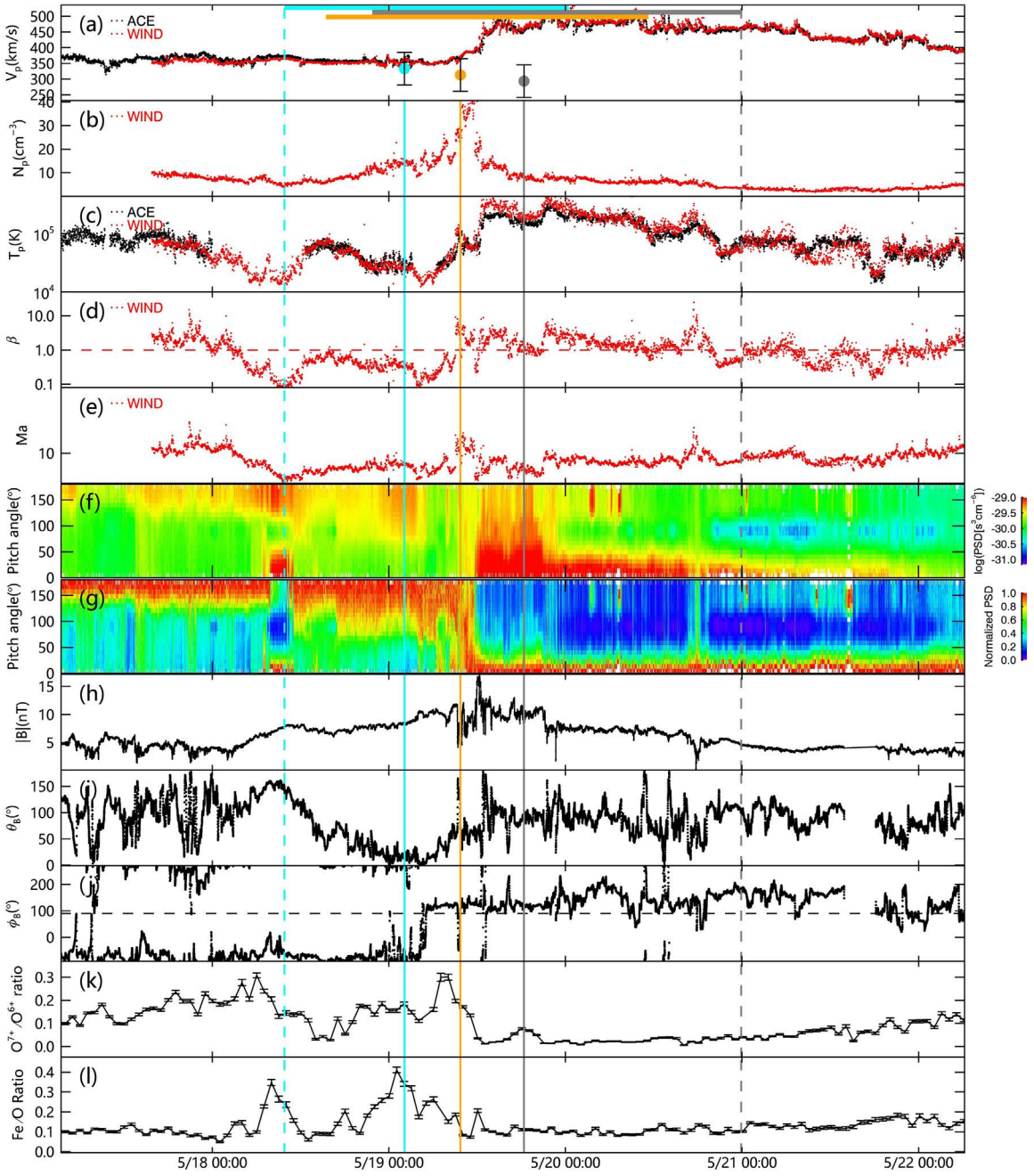


**Figure 9.** The solar wind properties measured in situ around the predicted arrival time of different parts of the case 2 transient.

Fe/O ratio from >0.3 to <0.1. For the second peak near P2, the magnetic field undergoes a reversal in direction for a brief period, and the $O^{7+}/O^{6+}$ ratio increases from <0.1 to ∼0.4. The third peak in the vicinity of P3 is characterized by decreased $\beta$ and $M_a$, increased magnetic magnitude, and reversal of the magnetic field direction. The $O^{7+}/O^{6+}$ ratio increases again from <0.2 to 0.3, and the Fe/O ratio varies from 0.1 to 0.2. Following the third peak, the phase space density (PSD) of the suprathermal electrons is observed to be enhanced in the direction of PA < 90°. Figure 8 also clearly shows the passage of an SIR later on 20 January, characterized by an increase in the velocity and temperature, peak of the density, compressed magnetic field, and $O^{7+}/O^{6+}$ ratio. Ahead of the SIR, the spacecraft detected bidirectional electron strahl and rotated the magnetic field during January 20 02:00–08:30, accompanied by a drop in $T_p$ and $\beta$, and the PSD of suprathermal electrons is enhanced after this.

Figure 9 illustrates the in situ measurements surrounding the predicted arrival time for the event in case 2. Here, the predicted arrival times of P1, P2, and P3 at L1 are 2010 May 19 02:07 UTC, 2010 May 19 09:43 UTC, and 2010 May 19 18:22 UTC, respectively. We find that the predicted P2 in this case is located between fast and slow wind intervals, and the estimated velocity is close to the observed in situ speed of the SSW stream. A peak in density was detected at near May 19 10:00 UTC, indicating the compressed SIR region located between P1 and P3, and was associated with increased $T_p$ and reversed suprathermal electron strahl. Ahead of the SIR, the signature of a rotating magnetic field is detected during May 18 09:00–May 19 04:00, thereby suggesting the existence of a flux rope. During this period, $T_p$

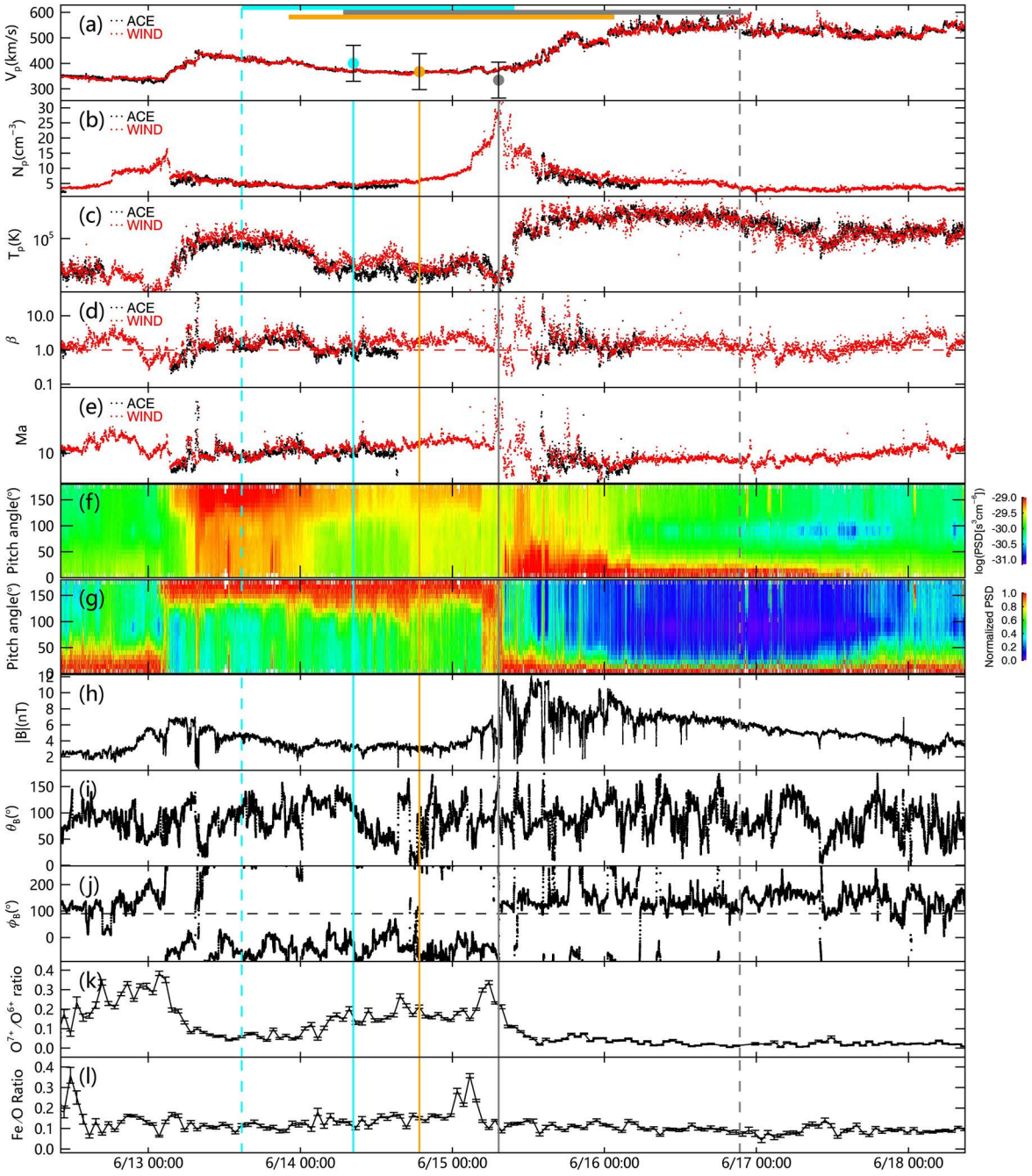


**Figure 10.** The solar wind properties measured in situ around the predicted arrival time of different parts of the case 3 event.

exhibits a decline and $\beta$ is <1, which is also consistent with the characteristics of large flux ropes (J. T. Gosling et al. 1973; L. Burlaga et al. 1981; R. P. Lepping et al. 1990; H. V. Cane & I. G. Richardson 2003). Bidirectional suprathermal electron strahls are detected at about May 18 07:00–10:00. The PSD of the suprathermal electrons decreases after a reversal of the magnetic field at about May 19 05:00 and is enhanced after the reversal of the electron strahl at about May 19 10:00, accompanied by a low $O^{7+}/O^{6+}$ ratio and Fe/O ratio. In the flux rope interval, the $O^{7+}/O^{6+}$ ratio and Fe/O ratio exhibit higher values proximate to the edges of the flux rope than those observed within the interval.

Figure 10 shows the in situ measurements related to the reconstructed event in case 3. Arrival times for P1, P2, and P3 for this event at the L1 point are predicted as 2010 June 14 08:22, 2010 June 14 18:48, and 2010 June 15 07:18, respectively. During June 12–18, the spacecraft detected three solar wind streams with different magnetic field polarities, and their boundaries are located at June 13 03:00 and June 15 07:00, respectively. The predicted arrival times of P1–P3 fall within the interval of the second stream, and the predicted velocity is close to the in situ measurement of 360–380 km s$^{-1}$. At the time of P2, the PSD of suprathermal electrons is enhanced. The elevation angle of the magnetic field varies during June 14 07:00–16:00, and a 2 hr field reversal is detected after that, as shown in panel (i). This reversal is accompanied by an increase in temperature and a decrease in electron strahl, and a magnetic field dropout accompanied by increased temperature is detected at the

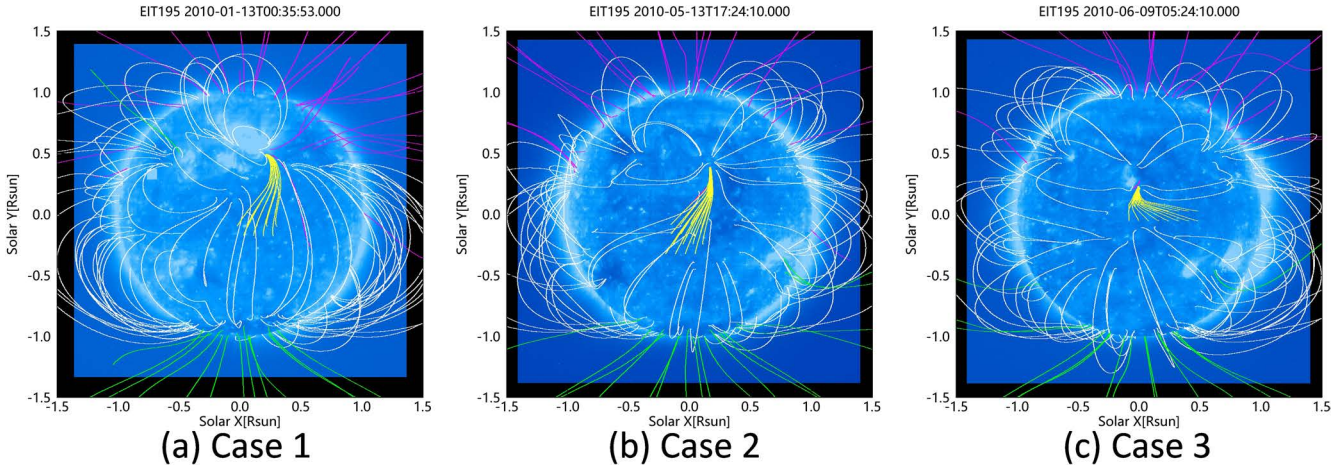


**Figure 11.** The possible solar origin of the transient and its ambient outflows in three cases of interest traced by the PFSS extrapolation of the photospheric magnetic field, as shown by the yellow lines. The background ultraviolet images are observed by SOHO/EIT at 195 Å, and the coronal field lines are derived by the PFSS programs in the SolarSoftWare system.

edge of the reversal. Concurrently, two SIRs were detected on June 13 and June 15, accompanied by increased velocity, enhanced number density, increased $T_p$, reversed and enhanced suprathermal electron strahls, compressed and reversed magnetic fields, and decreased $O^{7+}/O^{6+}$ ratios. The peaks in the Fe/O ratio appear shortly before the two SIRs.

### *3.4. Solar Origin of Transients with the Ambient Solar Wind*

To investigate further the in situ properties associated with these transients, we discuss the potential solar origin of the transient events and their ambient solar wind flows. Here we identify the source regions by tracing along the coronal magnetic field lines extrapolated by the PFSS model, as illustrated by the yellow lines in Figure 11. The extrapolation is derived from the photospheric magnetograms obtained by the Michelson–Doppler Imager (MDI; P. H. Scherrer et al. 1995) on board SOHO, and the background images are the EUV observations at 195 Å taken by the Extreme-ultraviolet Imaging Telescope (EIT; J. P. Delaboudiniere et al. 1995). It is important to note that this is an estimate of the solar source of the transient flows. It is also possible that the plasma forming these transients is released from other footpoints. Panels (a1)−(a3) in Figure 12 show the overall photospheric magnetic field, in addition to the open-field regions and the PIL, in the three cases. The PFSS field lines connecting the transients to the solar surface are marked by orange lines, and their footpoints are labeled by orange crosses. In the remaining panels of Figure 12, we display the solar wind quantities mapped back to the height of the source surface at 2.5 $R_\odot$, which are connected to the solar surface by the black lines using the two-step ballistic back-mapping technique (J. T. Nolte & E. C. Roelof 1973).

As demonstrated in Figure 11(a), the case 1 transient is traced by the PFSS field line to a large active region in the northern hemisphere, recorded as AR 11040 by the National Oceanic and Atmospheric Administration. In Figure 12, we can see that the transient event and the ambient SSW stream detected in situ are both connected to the western edge of this active region with negative magnetic field polarity, which is consistent with the in situ measurement of the magnetic field polarity shown in Figure 12(b1). The subsequent SSW and FSW streams exhibiting positive polarity, in conjunction with the SIR between them, are connected to the small open-field region situated at approximately 200° in longitude, where the PIL extends into the northern hemisphere. The tilted PIL crosses the equatorial plane at about 212° in longitude, which is located between the solar wind streams with different magnetic field polarities.

In case 2, the transient event is located near the PIL, and the ambient flow for this event is traced to the low-latitude coronal hole situated between 90° and 100° in longitude, as shown in Figures 11(b) and 12(a2). The compressed SIR region detected in situ is mapped back to the height of the source surface at about 70°−80° in longitude, near the equatorial position of the tilted PIL at approximately 62° in longitude. Prior to the SIR, the SSW, accompanied by negative polarity and a high $O^{7+}/O^{6+}$ ratio, is traced to the same source region as the event. After the SIR, the FSW accompanied by positive polarity and a low $O^{7+}/O^{6+}$ ratio is primarily connected to the southern coronal hole extending toward the low-latitude region at approximately 30° in longitude with the same polarity.

The case 3 event is traced back to the boundary of a small active region, as shown in Figure 11(c). As illustrated in Figures 12(a3) and (b3), the longitude of this event is close to its low-latitude source region located at approximately 90° in longitude, accompanied by the same negative polarity detected in situ. Due to the influence of this open-field source region, the PIL extends to 25°S in the southern hemisphere. The positions of the tilted PIL crossing the equator are about 45° and 127° in longitude, respectively. The compressed SIR, which is considered to entrain the case 3 event, is traced back to the region of about 70°–80° in longitude on the source surface. The SSW stream, detected in situ before 13 June with positive magnetic polarity, and the following stream, detected before June 15 with negative magnetic polarity, were connected to the same source region as the transient event. After June 15, the part of the FSW stream released ahead of the tilted PIL was traced to the equatorial open-field region at about 85° in longitude, and the part after the tilted PIL was traced to the southern coronal hole, which extends to low latitude at about 20° in longitude without apparent sunspots.

## 4. Discussion

Applying the tracing technique, we have established a connection between three remote transients identified by our

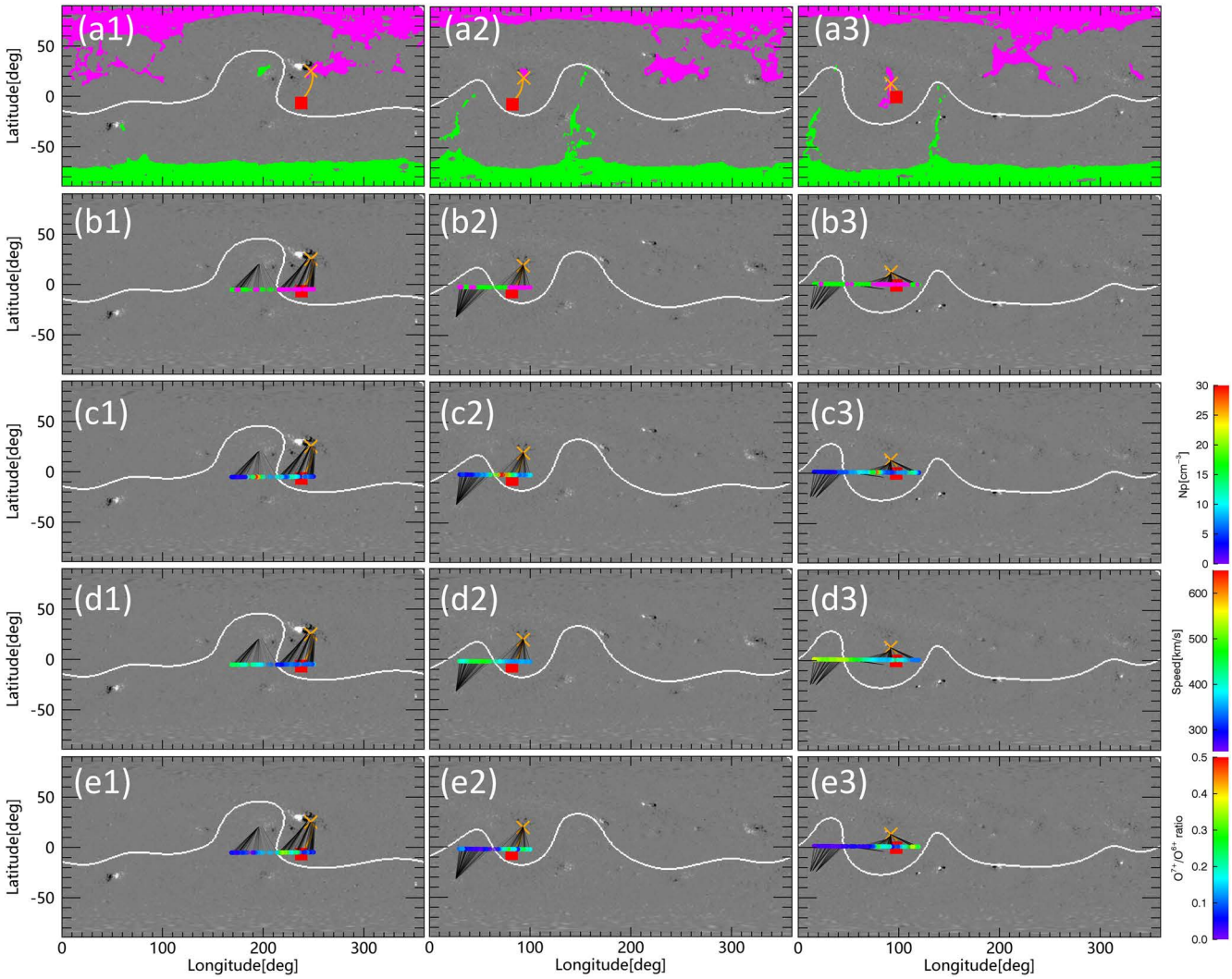


**Figure 12.** Panels (a1)−(a3): the Carrington maps of the photospheric magnetic field taken by SOHO/MDI in cases 1–3. The negative- (positive-) polarity open-field regions are labeled as the pink (green) regions. The positions of the events are marked by the red squares, and their possible source regions are labeled by the orange crosses. The white lines represent PILs. The panels in the following rows show the in situ quantities of solar wind mapped back to the source surface of the Sun at 2.5 $R_\odot$ and traced to the solar surface by the black lines: (b1)−(b3), magnetic field polarity labeled by the same colors as in panels (a1)−(a3); (c1)−(c3), proton number density; (d1)−(d3), solar wind velocity; and (e1)−(e3)$O^{7+}/O^{6+}$ ratio.

CORAR technique to the solar wind features measured at L1. The signatures detected in situ should be further discussed, combined with the remote observations and source analysis, to elucidate the credibility of their association with the transients.

In case 1, the in situ signatures suggest that the transient event can be associated with the high-density regions (HDRs) detected at L1. These HDRs are potentially substructures of the HPS located around the HCS, which is similar to scenario 3 of the HPS measurement described in E. Sanchez-Diaz et al. (2017a, 2019). The decrease in the suprathermal electron strahl accompanied by the HDRs suggests the passage of magnetic field lines disconnected from the Sun (D. J. McComas et al. 1989; J. T. Gosling et al. 2005; N. U. Crooker & C. Pagel 2008; A. P. Rouillard et al. 2010). The enhancement of suprathermal electron strahls after HDRs is expected to arise from the magnetic compression and the increase of the suprathermal electron density or from the connection of magnetic field lines to the coronal hole (N. U. Crooker et al. 2010; A. R. Macneil et al. 2020). The variation of $O^{7+}/O^{6+}$ ratios indicates that the SSW around the last two HDRs may originate from different source regions from the first HDR. Y. M. Wang et al. (2009) suggested that the SSW with high ion charge ratios comes from active regions heating ions in the low corona. Conversely, the SSW exhibiting intermediate $O^{7+}/O^{6+}$ and Fe/O ratios may originate from the polar-hole boundaries characterized by weaker low coronal heating. Combining the in situ and remote observations, we suggest that the plasma related to this transient is first released from the open-field boundary of the active region observed on the Sun and then ejected from the tip of the closed field above the active region AR 11040. The involvement of this large active region may explain the higher ion charge ratios detected in case 1 (0.3–0.4) than the other two cases (<0.3). In addition to the transient, the slow and fast streams generating the SIR after the case 1 transient have the same polarity. The following FSW is released from the small low-latitude hole, while the SSW before the SIR is possibly released from the boundary of the positive-polarity part of the active region by interchange reconnection.

The in situ features suggest that the case 2 transient observed in the corona is connected to a high-density core generated at the rear of a large flux rope, which is subsequently

compressed by an SIR. It has been identified as an ICME in the WIND catalog.[5] Considering the position, size, and shape of this event, it may be the bright core of a slow streamer blowout event, which is characterized by a gradual swelling of the overlying streamer and released from the filaments above the PIL (N. R. Sheeley et al. 1982; A. Vourlidas & D. F. Webb 2018; T. Nieves-Chinchilla et al. 2020). Its loop-like feature is also observed in the COR1 FOV. It appears to be a narrow CME with its initial angular width smaller than 15° (H. R. Gilbert et al. 2001; S. Yashiro et al. 2003; N. Mittal et al. 2009) in the corona. H. R. Gilbert et al. (2001) analyzed 15 narrow CME events and found that most of them could be traced to a sharp bending in the PIL, which is also present in this case. The latitudinal expansion observed in the heliosphere suggests that this event may be deflected or rotated during propagation, perhaps due to the interaction with the ambient solar wind and the influence of the ambient magnetic field (T. Nieves-Chinchilla et al. 2012; Y. D. Liu et al. 2013; S. Kumar et al. 2024). The increase of Fe/O ratio indicates the elevation of the FIP bias. Statistical studies have revealed that the charge states, helium abundance, and FIP bias of ICMEs are generally higher than those inside the background solar wind (I. G. Richardson & H. V. Cane 2004, 2010; M. J. Owens 2018; H. Song & S. Yao 2020; H. Song et al. 2021; X. Shi et al. 2022). Nevertheless, it has been demonstrated that some ICMEs from prominences can contain a cold component with lower charge states (X. Feng et al. 2018; J. Wang et al. 2018; D. Li & S. Yao 2020), which may explain the lower value of $O^{7+}/O^{6+}$ observed inside the flux rope.

According to the remote observation of the interplanetary solar wind, the transient event in case 3 fades during propagation, and its plasma material may become a part of the SIR-compressed outflow that appears to decelerate during propagation. Despite the detection of enhanced electron strahl at P2, concomitant with a changed magnetic field, it is uncertain whether they are correlated with the case 3 transient. The in situ signatures observed at P2 may be attributed to the magnetic reconnection process during the propagation of the solar wind (T. D. Phan et al. 2021; P. C. Liewer et al. 2024). The magnetic field dropout and enhanced temperature at the edge of the field reversal near P2 indicate the existence of reconnection exhausts. The enhancement of suprathermal electrons at P2 is likely to be generated by the acceleration of electrons by magnetic reconnection or related to the magnetic field lines connected to the Sun. The back-mapping result indicates that the SSW and FSW, which generate the SIR carrying the case 3 event, are traced to the open-field boundary of a small active region. Given the observed deceleration of the SIR, it can be deduced that the actual longitude of the separation layer between FSW and SSW on the source surface is likely to be less than that of the back-mapping position, and the separation layer should be closer to the position of the tilted PIL.

The scale of the reconstructed transients, both in terms of latitude and longitude, is taken into account during the implementation of the tracing technique. It is important to note that the CORAR technique aims to reconstruct the visible part of the transient in images, and the real transient may have a larger size in radial distance and latitude than the observed feature and the reconstructed structure. In S. Lyu et al. (2023), it was found that the reconstruction performance of a small transient with clear features in COR2 images is influenced by the relative position of a transient to the two spacecraft. A test of the reconstruction of synthetic blobs on the meridian plane shows that when the angle between lines connecting the transient and two spacecraft ($\theta_{\rm blob}$) is about 130°–150°, similar to the condition of the three cases here, the ratio between the longitudinal width from reconstruction and the real size is about 0.6–1.1 and increases as $\theta_{\rm blob}$ grows. The findings of the test suggest that these small-scale transient events are likely to have a larger longitudinal size than their reconstructed structures. Consequently, the uncertainty of reconstruction in our cases appears to have minimal impact on our prediction result.

In case 1, the predicted trajectory of the transient does not match precisely the observed trace in the J map from STEREO-B. This discrepancy may be attributable to the distinct characteristics of the transient structure observed from different lines of sight (LOSs; N. R. Sheeley et al. 2009) or the potential obscurity of the case 1 event due to the presence of other transient flows along the LOS from STEREO-B. It is noteworthy that the uncertainty of the predicted arrival time at L1 can be larger than 20 hr, transferred from the prediction errors of the fitted velocity profiles with a 90% confidence interval. This highlights the significant variability in the SSW (D. J. McComas et al. 2008), which indicates that the embedded transients may interact with the surrounding flows at different speeds, thereby transferring the momentum between them (G. Lapenta & A. L. Restante 2008). Furthermore, if transients are entrained by SIRs (N. R. Sheeley & A. P. Rouillard 2010), the drag force exerted by the fast flow may accelerate the forward SSW transients and enhance their densities. Meanwhile, the predicted arrival of the edges of the reconstructed transients may be about 12 hr ahead of/behind its center, beyond the temporal scale of mesoscale transients. It is based on the assumption that transients expand constantly with the propagating solar wind, which may be unsuitable for interplanetary transients (Y. M. Wang et al. 2015). The unexpected nonradial flow detected by PSP (J. C. Kasper et al. 2019) also suggests that the hypothesis of radial propagation of transients may be invalid in the extended corona. In general, our tracking technique utilized in this study is capable of predicting the trajectory of small transients or their relative plasma materials embedded in the background SSW, while the complex evolution of the solar wind and the limitations on the fine observation of interplanetary small transients make it difficult to confirm the prediction.

## 5. Summary

In this study, a data set of solar wind transients at small scales is obtained from the CORAR reconstruction for the period from 2010 January to July. The analysis focused on three cases of reconstructed transients that were traveling toward the Earth. The 3D trajectories of these transients were extrapolated into the heliosphere using single-vantage observations from STEREO-A. We find that the transients detected by our CORAR technique can be traced using remote observations into interplanetary space and detected in situ by the spaceborne observatories at the L1 point of the Sun–Earth line. The three transient events examined here are ejected from the vicinity of the tilted positions of the HCS. The event in case 1 is connected to the HDRs embedded within the HPS. It

[5] wind.nasa.gov/ICME_catalog/

is observed approximately 2 days ahead of an SIR, which is generated by the interaction between the fast and slow wind with the same positive polarity. In case 2, it is possible that the transient event is the bright core of a narrow and slow streamer blowout CME, accompanied by the presence of cold components within the flux rope and entrained by the SIR. The remote observation indicates the possibility of deflection or rotation during its propagation in the heliosphere. For the case 3 event, there is a likelihood of its mixture with the compressed outflow of an SIR. The in situ measured properties associated with these events and their ambient plasma flows are consistent with their source regions on the solar surface, accompanied by the same magnetic field polarity.

This work is an attempt to establish an exact connection between small solar wind transients near the Sun and their features detected in situ by spacecraft, which can help in understanding the evolution of solar wind transients from the corona into the heliosphere. Future research may focus on studying the connection of the transient events from remote observations to the near-Sun observatories, such as PSP and Solar Orbiter (D. Müller et al. 2020). This strategy would serve to reduce the uncertainty of prediction and facilitate a more in-depth study of the evolution of transients closer to the Sun in the heliosphere.

## Acknowledgments

We acknowledge the use of the data from STEREO/SECCHI, which are produced by a consortium of RAL (UK), NRL (USA), LMSAL (USA), GSFC (USA), MPS (Germany), CSL (Belgium), IOTA (France), and IAS (France). The SECCHI data can be found in the STEREO Science Center (https://stereo-ssc.nascom.nasa.gov/data/ins_data/secchi/). The ACE and WIND data are openly available at the Coordinated Data Analysis Workshop Web (CDAWeb; https://cdaweb.gsfc.nasa.gov/). We acknowledge the use of EIT and MDI data provided by SOHO, a project of international cooperation between ESA and NASA. The EIT images have been enhanced using a technique developed by Dr. Guillermo Stenborg. This work utilizes GONG data obtained by the NSO Integrated Synoptic Program, managed by the National Solar Observatory, which is operated by the Association of Universities for Research in Astronomy (AURA), Inc., under a cooperative agreement with the National Science Foundation and with contributions from the National Oceanic and Atmospheric Administration. This work is supported by the National Natural Science Foundation of China (42188101) and the Informatization Plan of the Chinese Academy of Sciences (CAS-WX2022SF-0103). The work of C.J.O. at the UCL/Mullard Space Science Laboratory is currently supported by STFC grant Nos. ST/W001004/1 and ST/X/002152/1. We acknowledge the support from the National Space Science Data Center, National Science and Technology Infrastructure of China (http://www.nssdc.ac.cn), and the support from the China Scholarship Council.

## ORCID iDs

Shaoyu Lyu https://orcid.org/0000-0002-2349-7940
Yuming Wang https://orcid.org/0000-0002-8887-3919
Christopher J. Owen https://orcid.org/0000-0002-5982-4667

## References

Abbo, L., Ofman, L., Antiochos, S. K., et al. 2016, SSRv, 201, 55
Alzate, N., Di Matteo, S., Morgan, H., Viall, N., & Vourlidas, A. 2024, ApJ, 973, 130
Alzate, N., Morgan, H., & Di Matteo, S. 2023, ApJ, 945, 116
Alzate, N., Morgan, H., Viall, N., & Vourlidas, A. 2021, ApJ, 919, 98
Baker, D., Démoulin, P., Yardley, S. L., et al. 2023, ApJ, 950, 65
Barnard, L., & Owens, M. 2022, FrP, 10, 1005621
Brueckner, G. E., Howard, R. A., Koomen, M. J., et al. 1995, SoPh, 162, 357
Bunting, K. A., Barnard, L., Owens, M. J., & Morgan, H. 2024, ApJ, 961, 64
Bunting, K. A., & Morgan, H. 2023, SpWea, 21, e2023SW003448
Burlaga, L., Sittler, E., Mariani, F., & Schwenn, R. 1981, JGRA, 86, 6673
Cane, H. V., & Richardson, I. G. 2003, JGRA, 108, 1156
Chen, Y., Li, X., Song, H. Q., et al. 2009, ApJ, 691, 1936
Chitta, L. P., Seaton, D. B., Downs, C., DeForest, C. E., & Higginson, A. K. 2023, NatAs, 7, 133
Crooker, N. U., Appleton, E. M., Schwadron, N. A., & Owens, M. J. 2010, JGRA, 115, A11101
Crooker, N. U., Burton, M. E., Siscoe, G. L., et al. 1996, JGRA, 101, 24331
Crooker, N. U., Huang, C. L., Lamassa, S. M., et al. 2004, JGRA, 109, A03107
Crooker, N. U., & Pagel, C. 2008, JGRA, 113, A02106
DeForest, C. E., Howard, R. A., Velli, M., Viall, N., & Vourlidas, A. 2018, ApJ, 862, 18
DeForest, C. E., & Howard, T. A. 2015, ApJ, 804, 126
DeForest, C. E., Howard, T. A., & Tappin, S. J. 2011, ApJ, 738, 103
Delaboudiniere, J. P., Artzner, G. E., Brunaud, J., et al. 1995, SoPh, 162, 291
Di Matteo, S., Viall, N. M., Kepko, L., et al. 2019, JGRA, 124, 837
Dorrian, G. D., Breen, A. R., Davies, J. A., et al. 2010, SoPh, 265, 207–231
Edmondson, J. K. 2012, SSRv, 172, 209
Einaudi, G., Boncinelli, P., Dahlburg, R. B., & Karpen, J. T. 1999, JGRA, 104, 521
Endeve, E., Holzer, T. E., & Leer, E. 2004, ApJ, 603, 307
Endeve, E., Leer, E., & Holzer, T. E. 2003, ApJ, 589, 1040
Eyles, C. J., Harrison, R. A., Davis, C. J., et al. 2009, SoPh, 254, 387
Feng, X., Yao, S., Li, D., Li, G., & Yan, X. 2018, ApJ, 868, 124
Fox, N. J., Velli, M. C., Bale, S. D., et al. 2016, SSRv, 204, 7
Geiss, J., Gloeckler, G., & Vonsteiger, R. 1995, SSRv, 72, 49
Gershkovich, I., Lepri, S., Viall, N., Di Matteo, S., & Kepko, L. 2023, SoPh, 298, 89
Gilbert, H. R., Serex, E. C., Holzer, T. E., MacQueen, R. M., & McIntosh, P. S. 2001, ApJ, 550, 1093
Gloeckler, G., Cain, J., Ipavich, F. M., et al. 1998, SSRv, 86, 497
Gosling, J. T., Pizzo, V., & Bame, S. J. 1973, JGR, 78, 2001
Gosling, J. T., Skoug, R. M., McComas, D. J., & Smith, C. W. 2005, GeoRL, 32, L05105
Higginson, A. K., & Lynch, B. J. 2018, ApJ, 859, 6
Hou, C., He, J., Duan, D., et al. 2024a, NatAs, 8, 1246
Hou, C., Rouillard, A. P., He, J., et al. 2024b, ApJL, 968, L28
Howard, R. A., Moses, J. D., Vourlidas, A., et al. 2008, SSRv, 136, 67
Howard, T. A., & DeForest, C. E. 2012, ApJ, 746, 64
Kaiser, M. L., Kucera, T. A., Davila, J. M., et al. 2008, SSRv, 136, 5
Kasper, J. C., Bale, S. D., Belcher, J. W., et al. 2019, Natur, 576, 228
Kepko, L., & Spence, H. E. 2003, JGRA, 108, 1257
Kepko, L., Spence, H. E., & Singer, H. J. 2002, GeoRL, 29, 39
Kepko, L., Viall, N. M., Antiochos, S. K., et al. 2016, GeoRL, 43, 4089
Kepko, L., Viall, N. M., & Wolfinger, K. 2020, JGRA, 125, e2020JA028037
Kilpua, E. K. J., Luhmann, J. G., Gosling, J., et al. 2009, SoPh, 256, 327
Kumar, S., Srivastava, N., Gopalswamy, N., & Dash, A. 2024, ApJ, 977, 57
Lapenta, G., & Restante, A. L. 2008, AnGeo, 26, 3049
Leamon, R. J., Smith, C. W., Ness, N. F., Matthaeus, W. H., & Wong, H. K. 1998, JGRA, 103, 4775
Lepping, R. P., Acuna, M. H., Burlaga, L. F., et al. 1995, SSRv, 71, 207
Lepping, R. P., Jones, J. A., & Burlaga, L. F. 1990, JGRA, 95, 11957
Li, D., & Yao, S. 2020, ApJ, 891, 79
Li, H., Huang, Z., Deng, K., et al. 2024, A&A, 683, A126
Li, X., Wang, Y., Guo, J., Liu, R., & Zhuang, B. 2021, A&A, 649, A58
Li, X., Wang, Y., Liu, R., et al. 2020, JGRA, 125, e2019JA027513
Li, X., Wang, Y., Shen, F., et al. 2023, ApJ, 949, 58
Li, X. L., Wang, Y. M., Liu, R., et al. 2018, JGRA, 123, 7257
Liewer, P. C., Gallagher, B. M., Stenborg, G., et al. 2024, ApJ, 970, 79
Liu, Y. C. M., Qi, Z., Huang, J., et al. 2020, A&A, 635, A49
Liu, Y. D., Luhmann, J. G., Lugaz, N., et al. 2013, ApJ, 769, 45
Lynch, B. J., Viall, N. M., Higginson, A. K., et al. 2023, ApJ, 949, 14
Lyu, S., Li, X., & Wang, Y. 2020, AdSpR, 66, 2251
Lyu, S., Wang, Y., Li, X., & Zhang, Q. 2023, A&A., 672, A100
Lyu, S., Wang, Y., Li, X., Zhang, Q., & Liu, J. 2024, ApJ, 962, 170
Lyu, S., Wang, Y., Li, X., et al. 2021, ApJ, 909, 182
Macneil, A. R., Owen, C. J., Baker, D., et al. 2019, ApJ, 887, 146

Macneil, A. R., Owens, M. J., Berčič, L., & Finley, A. J. 2020, MNRAS, 498, 5273
Macneil, A. R., Owens, M. J., Finley, A. J., & Matt, S. P. 2022, MNRAS, 509, 2390
McComas, D. J., Bame, S. J., Barker, P., et al. 1998, SSRv, 86, 563
McComas, D. J., Ebert, R. W., Elliott, H. A., et al. 2008, GeoRL, 35, L18103
McComas, D. J., Gosling, J. T., Phillips, J. L., et al. 1989, JGRA, 94, 6907
Mittal, N., Pandey, K., Narain, U., & Sharma, S. S. 2009, Ap&SS, 323, 135
Müller, D., St. Cyr, O. C., Zouganelis, I., et al. 2020, A&A, 642, A1
Neugebauer, M., Liewer, P. C., Smith, E. J., Skoug, R. M., & Zurbuchen, T. H. 2002, JGRA, 107, 1488
Neugebauer, M., Forsyth, R. J., Galvin, A. B., et al. 1998, JGRA, 103, 14587
Nieves-Chinchilla, T., Colaninno, R., Vourlidas, A., et al. 2012, JGRA, 117, A06106
Nieves-Chinchilla, T., Szabo, A., Korreck, K. E., et al. 2020, ApJS, 246, 63
Nolte, J. T., & Roelof, E. C. 1973, SoPh, 33, 241
Ogilvie, K. W., Chornay, D. J., Fritzenreiter, R. J., et al. 1995, SSRv, 71, 55
Owens, M. J. 2018, SoPh, 293, 122
Owens, M. J., & Riley, P. 2017, SpWea, 15, 1461
Phan, T. D., Lavraud, B., Halekas, J. S., et al. 2021, A&A, 650, A13
Pizzo, V. J. 1981, JGRA, 86, 6685
Raouafi, N. E., Stenborg, G., Seaton, D. B., et al. 2023, ApJ, 945, 28
Reville, V., Velli, M., Rouillard, A. P., et al. 2020, ApJL, 895, L20
Réville, V., Fargette, N., Rouillard, A. P., et al. 2022, A&A, 659, A110
Richardson, I. G., & Cane, H. V. 2004, JGRA, 109, A09104
Richardson, I. G., & Cane, H. V. 2010, SoPh, 264, 189
Riley, P., & Lionello, R. 2011, SoPh, 270, 575
Riley, P., Gosling, J. T., McComas, D. J., et al. 1999, JGRA, 104, 9871
Robbrecht, E., Berghmans, D., & Van der Linden, R. A. M. 2009, ApJ, 691, 1222
Rouillard, A. P., Davies, J. A., Forsyth, R. J., et al. 2008, GeoRL, 35, L10110
Rouillard, A. P., Savani, N. P., Davies, J. A., et al. 2009, SoPh, 256, 307
Rouillard, A. P., Lavraud, B., Davies, J. A., et al. 2010, JGRA, 115, A04104
Sanchez-Diaz, E., Rouillard, A. P., Davies, J. A., et al. 2017a, ApJ, 851, 32
Sanchez-Diaz, E., Rouillard, A. P., Lavraud, B., Kilpua, E., & Davies, J. A. 2019, ApJ, 882, 51
Sanchez-Diaz, E., Rouillard, A. P., Davies, J. A., et al. 2017b, ApJ, 835, L7
Scherrer, P. H., Bogart, R. S., Bush, R. I., et al. 1995, SoPh, 162, 129
Schrijver, C. J., & DeRosa, M. L. 2003, SoPh, 212, 165
Schwenn, R. 2006, SSRv, 124, 51
Sheeley, J. N. R., & Wang, Y. M. 2007, ApJ, 655, 1142
Sheeley, J. N. R., Wang, Y. -M, Hawley, S. H., et al. 1997, ApJ, 484, 472
Sheeley, N. R., Howard, R. A., Koomen, M. J., et al. 1982, SSRv, 33, 219
Sheeley, N. R., Lee, D. D. H., Casto, K. P., Wang, Y. M., & Rich, N. B. 2009, ApJ, 694, 1471
Sheeley, N. R., & Rouillard, A. P. 2010, ApJ, 715, 300
Sheeley, N. R., Walters, J. H., Wang, Y. M., & Howard, R. A. 1999, JGRA, 104, 24739
Shi, X., Fu, H., Huang, Z., Ma, C., & Xia, L. 2022, ApJ, 940, 103
Smith, C. W., L'Heureux, J., Ness, N. F., et al. 1998, SSRv, 86, 613
Song, H., Li, L., Sun, Y., et al. 2021, SoPh, 296, 111
Song, H., & Yao, S. 2020, ScChE, 63, 2171
Ventura, R., Antonucci, E., Downs, C., et al. 2023, A&A, 675, A170
Viall, N. M., & Borovsky, J. E. 2020, JGRA, 125, e2018JA026005
Viall, N. M., DeForest, C. E., & Kepko, L. 2021, FrASS, 8, 139
Viall, N. M., Kepko, L., & Spence, H. E. 2008, JGRA, 113, A07101
Viall, N. M., Kepko, L., & Spence, H. E. 2009a, JGRA, 114, A01201
Viall, N. M., Spence, H. E., & Kasper, J. 2009b, GeoRL, 36, L23102
Viall, N. M., Spence, H. E., Vourlidas, A., & Howard, R. 2010, SoPh, 267, 175
Viall, N. M., & Vourlidas, A. 2015, ApJ, 807, 176
Vourlidas, A., & Webb, D. F. 2018, ApJ, 861, 103
Wang, J., Feng, H., & Zhao, G. 2018, A&A, 616, A41
Wang, Y. M., Ko, Y. K., & Grappin, R. 2009, ApJ, 691, 760
Wang, Y. M., Zhou, Z. J., Shen, C. L., Liu, R., & Wang, S. 2015, JGRA, 120, 1543
Wang, Y. M., Sheeley, J. N. R., Walters, J. H., et al. 1998, ApJ, 498, L165
Yashiro, S., Gopalswamy, N., Michalek, G., & Howard, R. A. 2003, AdSpR, 32, 2631